



Cite this: *Green Chem.*, 2025, **27**, 6796

## Asymmetric defective site-triggered triple synergistic modulation in nanoconfined aerogel for superior electrochemical conversion of low-concentration nitrate into ammonia †

Ke Wang, Tong Zhao, Shiyu Zhang, Rupeng Wang, Meng Wang, Zixiang He and Shih-Hsin Ho  \*

Electrocatalytic conversion of low-concentration nitrate ( $\text{NO}_3^-$ ) into ammonia ( $\text{NH}_3$ ) under ambient conditions is expected to provide an effective solution to the global nitrogen cycle imbalance. However, this process is hindered by slow reaction kinetics and the competing hydrogen evolution reaction (HER). Herein, we anchored oxygen vacancy-containing hollow  $\text{Co}_3\text{O}_4$  nanoparticles on waste spirulina residue-derived reduced graphene oxide aerogel ( $\text{Vo-HCo}_3\text{O}_4@\text{SRGA}$ ) for electrocatalytic low-concentration  $\text{NO}_3^-$  reduction. Finite element simulation demonstrates that the nanoconfined SRGA significantly increases the local concentration of  $\text{NO}_3^-$ , thereby accelerating the reaction kinetics. Moreover, the Vo is able to disrupt the local structural symmetry of  $\text{Co}-\text{O}-\text{Co}$  sites. The asymmetric active site (Vo) can simultaneously enhance  $\text{NO}_3^-$  adsorption, promote water dissociation, and inhibit hydrogen evolution. Thanks to the triple synergistic modulation of Vo and the nanoconfined effect of SRGA,  $\text{Vo-HCo}_3\text{O}_4@\text{SRGA}$  exhibits unprecedented activity ( $\text{NH}_3\text{-N}$  yield rate:  $1.53 \text{ mg h}^{-1} \text{ cm}^{-2}$ ;  $\text{NH}_3\text{-N}$  Faraday efficiency: 96.5%) superior to most of the reported advanced electrocatalysts under low-concentration  $\text{NO}_3^-$  conditions. This work cleverly combines macroscopic modification with microscopic fine tuning of catalysts, which is expected to open up new opportunities in the direction of pollutant resourcing.

Received 16th February 2025,  
Accepted 12th May 2025

DOI: 10.1039/d5gc00830a  
[rsc.li/greenchem](http://rsc.li/greenchem)

### Green foundation

1. This work provides an efficient solution for low-concentration nitrate reduction and ammonia synthesis under ambient conditions. By utilizing oxygen vacancy-rich hollow  $\text{Co}_3\text{O}_4$  nanoparticles anchored on waste spirulina residue-derived graphene oxide aerogel ( $\text{Vo-HCo}_3\text{O}_4@\text{SRGA}$ ), the combined effects of oxygen vacancies and confinement accelerate reaction kinetics, offering an energy-efficient solution for wastewater treatment and resource recovery. Importantly, the preparation process uses only deionized water instead of toxic organic solvents, making it more environmentally friendly.
2. The catalyst achieves an  $\text{NH}_3\text{-N}$  yield rate of  $1.53 \text{ mg h}^{-1} \text{ cm}^{-2}$  and a Faraday efficiency of 96.5%, outperforming many previously reported electrocatalysts.
3. Future research will focus on replacing traditional power sources with solar panels, using renewable energy to create a zero-carbon system for sustainable nitrogen management.

## 1. Introduction

Nitrate ( $\text{NO}_3^-$ ) has been widely present in industrial wastewater and groundwater in recent years as a result of industrial emissions and agricultural fertilization, and its excessive emission and accumulation can disrupt ecological balance and the global nitrogen cycle.<sup>1–3</sup> The electrocatalytic nitrate reduction

reaction ( $\text{eNO}_3^-$ -RR) enables the conversion of aqueous  $\text{NO}_3^-$  pollutants into value-added ammonia ( $\text{NH}_3$ ) using renewable electricity.<sup>4–7</sup> This approach represents a sustainable win-win strategy for environmental remediation and chemical production. The main research direction of the  $\text{eNO}_3^-$ -RR at present focuses on the exploration of the ideal conditions of high alkaline electrolyte and high  $\text{NO}_3^-$  concentration.<sup>8–11</sup> Unfortunately, it is almost impossible to find ideal scenarios with both high alkalinity and high  $\text{NO}_3^-$  concentration in authentic polluted waters, greatly blocking the feasibility of  $\text{eNO}_3^-$ -RR technology in practical applications.<sup>12</sup> Noteworthily, the majority of authentic contaminated water bodies around the globe are typically at low  $\text{NO}_3^-$  concentration levels

State Key Laboratory of Urban Water Resource and Environment, School of Environment, Harbin Institute of Technology, Harbin, 150040, P. R. China.  
 E-mail: stephen6949@hit.edu.cn

† Electronic supplementary information (ESI) available. See DOI: <https://doi.org/10.1039/d5gc00830a>

( $\leq 10$  mM) with near-neutral pH values.<sup>13</sup> From a practical perspective, directly reducing the low concentration of  $\text{NO}_3^-$  also helps to avoid high energy consumption that is typically associated with separating and concentrating  $\text{NO}_3^-$ . However, the slow reaction kinetics is caused by the decrease in the number of reactant molecules and the reduced utilization of active sites at low  $\text{NO}_3^-$  concentrations. Furthermore, the competing hydrogen evolution reaction (HER) severely limits efficient  $\text{NO}_3^-$  conversion. Consequently, the development of suitable catalysts to overcome the aforementioned bottlenecks and enhance the  $\text{NH}_3$  yield rate and selectivity is a critical issue that requires immediate attention.

Inspired by the nanoconfined effect in natural biological systems (*i.e.*, the cytoskeleton), a remarkable increase in reaction speed and specificity for efficient chemistry is expected to be achieved *via* constructing artificial microscopic nanoconfined spaces.<sup>14–16</sup> Once reactants enter the nanoconfined space, reduced diffusion freedom significantly increases local concentration, thus accelerating the reaction kinetics.<sup>17–19</sup> For example, the nanoconfined effect through graphene aerogel can effectively enrich the reducing intermediates and promote the reduction of  $\text{Fe}(\text{III})$ , resulting in a 208-fold enhancement in the phenol degradation rate constant compared with a system without nanoconfinement.<sup>20</sup> Therefore, we envisage that the unavoidable slow kinetics at low  $\text{NO}_3^-$  concentrations can be expected to be solved by rationally designing an electrocatalytic system with nanoconfined effect. However, to the best of our knowledge, the application of the graphene aerogel-triggered nanoconfined effect in the  $\text{eNO}_3^-$ -RR has yet to be reported and validated.

In addition, the low catalytic activity due to the competitive HER cannot be ignored. An effective way to inhibit the HER is to regulate the adsorption and binding sites of the hydrogen proton ( $^*H$ ) on the surface of the catalysts. Usually, the asymmetric defect site (Vo) causes uneven spatial distribution of active sites, in turn leading to spatial mismatch between the adsorption and binding sites of  $^*H$ . This geometric constraint further prevents the proximity and recombination of two  $^*H$  intermediates into hydrogen.<sup>21</sup> Moreover, this spatial mismatch likewise raises the reactive energy barrier for hydrogen generation, thereby effectively inhibiting the HER.<sup>22,23</sup> In contrast, when  $^*H$  is adsorbed on active sites with a symmetric structure, the symmetric structure is capable of effectively lowering the reactive energy barrier for the HER through a uniformly distributed electron cloud. Proverbially, the  $\text{eNO}_3^-$ -RR requires a large amount of  $^*H$  to participate in the reaction, and these  $^*H$  originate from the dissociation of water molecules. The asymmetry of Vo leads to a distortion of the geometrical configuration of the water molecule *via* altering the local electronic environment and creating an asymmetric electric field. This effect weakens the O–H bond energy and enhances  $\text{H}_2\text{O}$  dissociation probability.<sup>24,25</sup> This asymmetric electric field also exerts a force on  $\text{NO}_3^-$ , leading to polarity induction and thus enhancing the adsorption process. Here, we uncovered a principal fact that Vo can enhance  $\text{NO}_3^-$  adsorption, promote water dissociation, and inhibit the HER.

Nevertheless, the current literature lacks sufficient information to support Vo-triggered triple synergistic modulation. Furthermore, it has also not been verified whether there is a synergistic co-operation between the nanoconfined effect and Vo.

Herein, we anchored Vo- $\text{HCo}_3\text{O}_4$  on the surface of the nanoconfined SRGA to address the kinetic limitations and competing HER issues for the electrocatalytic reduction of low concentrations of  $\text{NO}_3^-$  to  $\text{NH}_3$  under neutral conditions. Notably, the nanoconfined effect generated by the porous skeleton of SRGA significantly enhanced the local  $\text{NO}_3^-$  concentration, in turn effectively breaking through the slow bottleneck in the kinetic process. Then, the introduced Vo as an asymmetric active site induced a triple synergistic modulation: enhancement of  $\text{NO}_3^-$  adsorption, promotion of water dissociation and inhibition of the HER. Thanks to the synergistic co-operation of the above efficacies, the Vo- $\text{HCo}_3\text{O}_4$ @SRGA exhibits remarkable catalytic activity for the conversion of low-concentration  $\text{NO}_3^-$  into  $\text{NH}_3$ .

## 2. Experimental section

### 2.1. Chemicals

All chemical reagents are described in Text S1.<sup>†</sup>

### 2.2. Catalyst preparation

**2.2.1. Preparation of Co-MOF@SRGO hydrogels.** In a typical synthesis, 20 mg of spirulina-based reduced graphene oxide (SRGO) was first dispersed in 10 mL of deionized water and ultrasonicated for 1 h to ensure uniform dispersion. Then, 184 mg of  $\text{Co}(\text{CH}_3\text{COO})_2 \cdot 4\text{H}_2\text{O}$ , 184 mg of 2-methylimidazole (2-mIM), and 20 mg of carboxymethyl cellulose (CMC) were sequentially added into the SRGO dispersion. Subsequently, the mixture was vigorously processed using a high-speed dispersion machine for 30 min to allow *in situ* growth of the Co-MOF on SRGO to form a homogeneous Co-MOF@SRGO hydrogel. Finally, the Co-MOF@SRGO hydrogel was dialyzed in deionized water for 24 h to remove unreacted precursors and impurities, completing the purification process.

**2.2.2. Preparation of Vo- $\text{HCo}_3\text{O}_4$ @SRGA.** The purified Co-MOF@SRGO hydrogels were directly coated on the surface of carbon paper, with the dosage details provided in Table S1.<sup>†</sup> Following coating, the hydrogel-loaded carbon paper was freeze-dried for 12 h to obtain the Co-MOF@SRGO aerogel (SRGA). Subsequently, the Co-MOF@SRGA composite was pyrolyzed at 800 °C for 2 h under an argon atmosphere to obtain Co@SRGA. Finally, Co@SRGA was thermally treated in a pre-heated tube furnace (280 °C,  $\text{O}_2/\text{Ar}$  atmosphere) for 30, 90, and 180 min to synthesize Y- $\text{Co}_3\text{O}_4$ @SRGA, Vo- $\text{HCo}_3\text{O}_4$ @SRGA and H- $\text{Co}_3\text{O}_4$ @SRGA, respectively (Y and H represent yolk-shell and hollow structures, respectively). These self-standing electrodes were directly employed for subsequent electrochemical tests.

**2.2.3. Preparation of H- $\text{Co}_3\text{O}_4$ .** For comparison, commercial cobalt powder with nanoparticle sizes matching those in H- $\text{Co}_3\text{O}_4$ @SRGA was employed as a reference. Meanwhile, pure

$\text{H-Co}_3\text{O}_4$  was synthesized under identical conditions as  $\text{H-Co}_3\text{O}_4@\text{SRGA}$  but without SRGA incorporation, ensuring a controlled evaluation of the role of SRGA in structural evolution.

### 2.3. Preparation of working electrodes of $\text{H-Co}_3\text{O}_4$

First, 21.5 mg of  $\text{H-Co}_3\text{O}_4$  and 20  $\mu\text{L}$  of 5 wt% Nafion solution were dispersed in a mixture of 655  $\mu\text{L}$  of ethanol and 325  $\mu\text{L}$  of deionized water *via* 60 min ultrasonication to prepare a homogeneous ink. Subsequently, 80  $\mu\text{L}$  of the resulting ink was uniformly coated onto carbon paper (CP,  $1 \times 1 \text{ cm}^2$ ) and air-dried at room temperature to complete the electrode fabrication.

### 2.4. Characterization

More details on the characterization methods are provided in the ESI (Text S2).†

### 2.5. Electrochemical measurements

The electrochemical measurements were conducted using a CHI 760e electrochemical workstation (Chenhua, Shanghai) in an H-type electrolytic cell. The as-prepared materials, Ag/AgCl electrode, and platinum foil were used as the working electrode, reference electrode, and counter electrode, respectively. The geometric area of the working electrode was set as  $1 \text{ cm}^2$ . 0.1 M  $\text{Na}_2\text{SO}_4$  solution (70 mL) was evenly distributed within the cathode and anode chambers, and  $\text{NaNO}_3$  was added into the cathode compartment containing  $140 \text{ mg L}^{-1} \text{NO}_3^-$ . All potentials were recorded against a reversible hydrogen electrode (RHE):

$$E_{\text{RHE}} = E_{\text{Ag/AgCl}} + 0.197 \text{ V} + 0.059 \text{ V} \times \text{pH}$$

Prior to the  $\text{NO}_3^-$  electroreduction test, the electrolyte was purged with high-purity Ar for 30 min. The scan rates for linear sweep voltammetry (LSV) tests and Tafel slope tests were maintained at  $10 \text{ mV s}^{-1}$ . Cyclic voltammetry (CV) curves acquired during electrochemical double-layer capacitance ( $C_{\text{dl}}$ ) determinations were measured in a potential window nearly without faradaic processes at different scan rates of 20, 40, 60, 80, and  $100 \text{ mV s}^{-1}$ . The plot of current density at a given potential against scan rate has a linear relationship, and its slope is  $C_{\text{dl}}$ . Electrochemical impedance spectra (EIS) were measured in a frequency domain ranging from 10 kHz to 0.1 Hz with a 5 mV perturbation. The chronoamperometry tests were conducted at a series of applied potentials.

### 2.6. Analytical methods

Detailed information on the determination of nitrogen species concentrations and the calculation of  $\text{eNO}_3^-$ -RR parameters is provided in Text S3 and Text S4,† respectively. Detailed steps of *in situ* Fourier transformed infrared (FT-IR) spectroscopy and online differential electrochemical mass spectrometry (DEMS) measurements are described in Text S5 and Text S6,† respectively. Detailed information on finite element method (FEM) simulations and density functional theory (DFT) calculations are presented in Text S7 and Text S8,† respectively.

## 3. Results and discussion

### 3.1. Catalyst characterization

SRGA was prepared according to our previously reported work (Fig. S1†). The preparation procedure for *in situ* growth of  $\text{Vo-HCo}_3\text{O}_4@\text{SRGA}$  on carbon paper is shown in Fig. 1a. First, the Co-MOF@SRGA hydrogel was uniformly coated on the surface of carbon paper, and then freeze-dried to obtain Co-MOF@SRGA (Fig. S2†). Subsequently, the obtained Co-MOF@SRGA was subjected to argon pyrolysis (Co@SRGA) and slow oxidation in air to obtain  $\text{Vo-HCo}_3\text{O}_4@\text{SRGA}$ . In addition, we optimized the loading amounts of  $\text{Vo-HCo}_3\text{O}_4@\text{SRGA}$  on the carbon paper (Fig. S3 and S4†). Scanning electron microscopy (SEM) images clearly demonstrate that  $\text{Vo-HCo}_3\text{O}_4$  nanoparticles present a highly dispersed distribution in the SRGA backbone without significant agglomeration (Fig. 1b and c and Fig. S5a†). In contrast, pure  $\text{Vo-HCo}_3\text{O}_4$  undergoes significant sintering under the same conditions (Fig. S5b†), suggesting that the three-dimensional porous network of SRGA limits the migration of  $\text{Vo-HCo}_3\text{O}_4$  particles, thus enhancing the structural stability of  $\text{Vo-HCo}_3\text{O}_4@\text{SRGA}$ . Transmission electron microscopy (TEM) images reveal that  $\text{Vo-HCo}_3\text{O}_4$  is discretely embedded on the surface of SRGA in the form of hollow nanoparticles with a diameter of approximately 20 nm (Fig. 1d). High-resolution TEM (HRTEM) images show that  $\text{Vo-HCo}_3\text{O}_4$  exhibited well-defined lattice diffraction fringes with a lattice spacing of 2.43 Å, consistent with the (311) plane of  $\text{Co}_3\text{O}_4$  (Fig. 1e). Additionally,  $\text{Vo-HCo}_3\text{O}_4$  contains uniformly distributed elements of Co and O, with the C

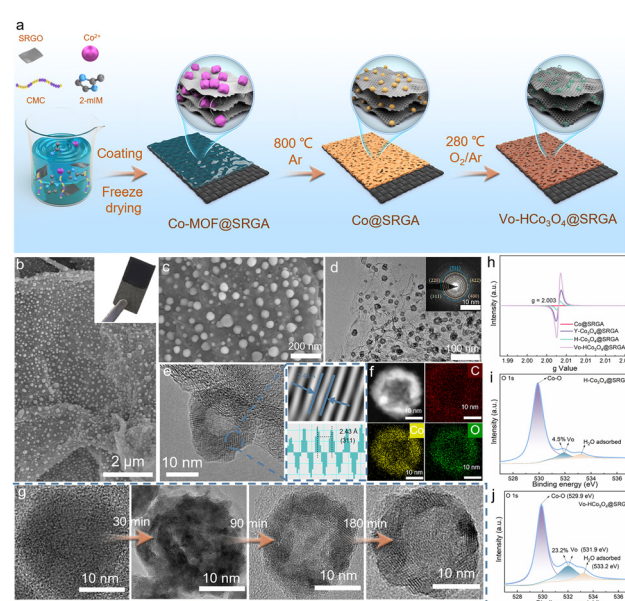


Fig. 1 (a) Schematic illustration of the preparation of  $\text{Vo-HCo}_3\text{O}_4@\text{SRGA}$ . (b and c) SEM, (d) TEM, (e) HRTEM, and (f) elemental mapping images of  $\text{Vo-HCo}_3\text{O}_4@\text{SRGA}$ . (g and h) TEM and EPR images of Co@SRGA, Y- $\text{Co}_3\text{O}_4$ @SRGA (30 min), Vo- $\text{HCo}_3\text{O}_4$ @SRGA (90 min), and H- $\text{Co}_3\text{O}_4$ @SRGA (180 min). (i and j) High-resolution XPS of O 1s of  $\text{H-Co}_3\text{O}_4@\text{SRGA}$  and  $\text{Vo-HCo}_3\text{O}_4@\text{SRGA}$ .

element dispersed throughout the entire  $\text{Vo-HCo}_3\text{O}_4$  structure (Fig. 1f). In order to reveal the evolution of the hollow structure of  $\text{Vo-HCo}_3\text{O}_4$ ,  $\text{Co@SRGA}$  formed by pyrolysis under an argon atmosphere was oxidized in air for different times. As shown in Fig. 1g,  $\text{Co@SRGA}$  underwent an evolutionary process from solid to yolk-shell to a completely hollow structure. This interesting structural evolution process can be explained *via* the Kirkendall effect.<sup>26</sup> Similarly, solid commercial Co nanoparticles were able to form hollow structures *via* the Kirkendall effect (Fig. S6†).

X-ray diffraction (XRD) and Raman images further confirmed the formation of  $\text{Co@SRGA}$  consisting of a pure metallic Co phase,  $\text{Y-Co}_3\text{O}_4@\text{SRGA}$  consisting of a mixed phase of metallic Co and  $\text{Co}_3\text{O}_4$ , and  $\text{Vo-HCo}_3\text{O}_4@\text{SRGA}$  and  $\text{H-Co}_3\text{O}_4@\text{SRGA}$  consisting of a pure  $\text{Co}_3\text{O}_4$  phase (Fig. S7†). In addition to the formation of hollow structures, the Kirkendall effect can produce structural disequilibria in metal oxides through the difference in diffusion rates between the metal and the oxygen, thus contributing to the generation of  $\text{Vo}^{27}$ . Electron paramagnetic resonance (EPR) techniques were applied to probe the presence of  $\text{Vo}$  in catalysts.  $\text{Vo-HCo}_3\text{O}_4@\text{SRGA}$  exhibited the highest EPR signal intensity, suggesting that the concentration of  $\text{Vo}$  could be effectively controlled by adjusting the oxidation times (Fig. 1h). The high-resolution X-ray photoelectron spectroscopy (XPS) of O 1s demonstrated that  $\text{Vo-HCo}_3\text{O}_4@\text{SRGA}$  (90 min) can reach the highest  $\text{Vo}$  content of 23.2%, which was higher than that for  $\text{H-Co}_3\text{O}_4@\text{SRGA}$  (180 min) of 4.5% and  $\text{Y-Co}_3\text{O}_4@\text{SRGA}$  (30 min) of 13.1% (Fig. 1i and j and Fig. S8a†). These results demonstrate that the controlled adjustment of oxidation time enables precise construction of different  $\text{Vo}$  concentrations in the catalysts. Meanwhile, according to the fine-scanned Co 2p XPS spectra, similarly high atomic ratios of  $\text{Co}^{2+}/\text{Co}^{3+}$  can be observed in  $\text{Y-Co}_3\text{O}_4@\text{SRGA}$  (1.16) and  $\text{Vo-HCo}_3\text{O}_4@\text{SRGA}$  (1.34), which are ascribed to the incompletely oxidized conditions, being consistent with the large number of  $\text{Vo}$  (Fig. S8b–d†). In sharp contrast, the atomic ratio of  $\text{Co}^{2+}/\text{Co}^{3+}$  in  $\text{H-Co}_3\text{O}_4@\text{SRGA}$  decreases to 1.05 because of the oxidation of  $\text{Co}^{2+}$  to  $\text{Co}^{3+}$ , leading to the decrease of  $\text{Vo}$ . The above analyses are consistent with the EPR results, indicating that  $\text{Vo-HCo}_3\text{O}_4@\text{SRGA}$  indeed has the highest concentration of  $\text{Vo}$ . In addition, the  $\text{Vo}$  content of  $\text{H-Co}_3\text{O}_4$  (5.1%) was not significantly different from that of  $\text{H-Co}_3\text{O}_4@\text{SRGA}$ , indicating that the introduction of SRGA did not affect the  $\text{Vo}$  content (Fig. S9†). The photoluminescence (PL) intensity of  $\text{Vo-HCo}_3\text{O}_4@\text{SRGA}$  is significantly lower than that of  $\text{HCo}_3\text{O}_4@\text{SRGA}$ . This suppression of radiative recombination is attributed to the presence of oxygen vacancies, which serve as electron-trapping centres and effectively inhibit the recombination of electron–hole pairs (Fig. S10†). As shown in Fig. S11,† the work function of  $\text{Vo-HCo}_3\text{O}_4@\text{SRGA}$  was significantly lower than that of  $\text{H-Co}_3\text{O}_4@\text{SRGA}$ , implying that the introduction of  $\text{Vo}$  can reduce the work function of the catalysts, thus enhancing the conductivity and reaction activity.<sup>28</sup> The introduction of SRGA greatly extended the specific surface area of  $\text{H-Co}_3\text{O}_4@\text{SRGA}$  and  $\text{Vo-HCo}_3\text{O}_4@\text{SRGA}$  compared with

$\text{H-Co}_3\text{O}_4$ , providing theoretical support for the enrichment of  $\text{NO}_3^-$  through the nanoconfined effect (Fig. S12 and Table S2†). In addition, we measured the adsorption capacity of the three catalysts to elucidate the nanoconfined effect of the SRGA framework on  $\text{NO}_3^-$ . As shown in Fig. S13 and Table S3,† compared with the correlation coefficient values  $R^2$  of the two kinetic models, the pseudo-second-order kinetic model was closer to the experimental data than the pseudo-first-order kinetic model, suggesting that the adsorption process of  $\text{NO}_3^-$  by the three materials was consistent with the pseudo-second-order kinetic hypothesis. The adsorption capacity and kinetic constants of  $\text{H-Co}_3\text{O}_4@\text{SRGA}$  were 2.4 times and 1.9 times those of  $\text{H-Co}_3\text{O}_4$ , respectively. Therefore, SRGA showed an obvious nanoconfined effect on  $\text{NO}_3^-$ , increased the local concentration of  $\text{NO}_3^-$  on the catalyst surface, and promoted the reaction kinetics of the electric reduction of  $\text{NO}_3^-$  to  $\text{NH}_3$ .

### 3.2. Electrocatalytic performance for the $\text{NO}_3^-$ -RR

To evaluate the impact of  $\text{Vo}$  and the nanoconfined effect of SRGA on the  $\text{eNO}_3^-$ -RR performance, LSV tests were initially conducted in an H-type electrolytic cell.  $\text{NO}_3^-$ ,  $\text{NO}_2^-$ , and the product  $\text{NH}_3$  were detected using an ultraviolet-visible (UV-vis) spectrophotometer (Fig. S14–S16†). The current density of  $\text{Vo-HCo}_3\text{O}_4@\text{SRGA}$  with the highest  $\text{Vo}$  concentration in the  $\text{NO}_3^-$  electrolyte was greater than that of  $\text{H-Co}_3\text{O}_4@\text{SRGA}$ ,  $\text{Co@SRGA}$ , and  $\text{Y-Co}_3\text{O}_4@\text{SRGA}$ , indicating that  $\text{Vo}$  can effectively enhance the  $\text{eNO}_3^-$ -RR process (Fig. 2a). Additionally, the current density of  $\text{H-Co}_3\text{O}_4$  was found to be significantly

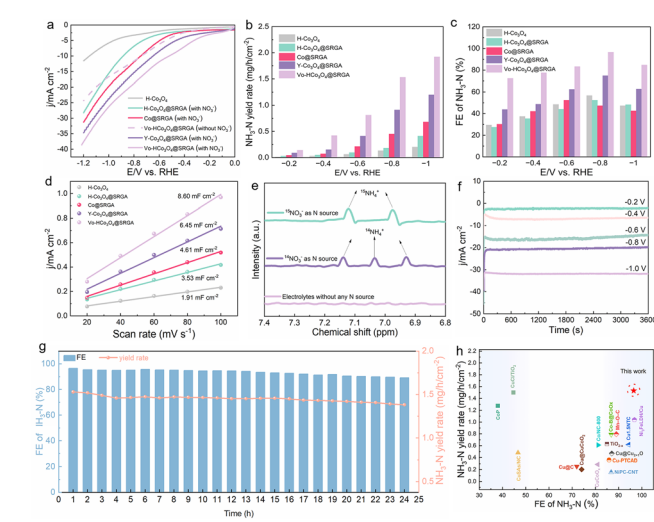


**Fig. 2** (a) LSV curves, (b)  $\text{NH}_3\text{-N}$  yield rates, (c) FE, and (d) the fitted linear relationship between the current density and the scan rate of  $\text{H-Co}_3\text{O}_4$ ,  $\text{H-Co}_3\text{O}_4@\text{SRGA}$ ,  $\text{Co@SRGA}$ ,  $\text{Y-Co}_3\text{O}_4@\text{SRGA}$ , and  $\text{Vo-HCo}_3\text{O}_4@\text{SRGA}$ . (e)  $^1\text{H}$ -NMR results for  $\text{NH}_4^+$  using  $^{14}\text{NO}_3^-$  and  $^{15}\text{NO}_3^-$  as the N source. (f) The  $i$ - $t$  curves of the  $\text{Vo-HCo}_3\text{O}_4@\text{SRGA}$  at various work potentials. (g) Cyclic stability test of  $\text{Vo-HCo}_3\text{O}_4@\text{SRGA}$ . (h) Comparison of the  $\text{eno}_3^-$ -RR performance for  $\text{Vo-HCo}_3\text{O}_4@\text{SRGA}$  with some related electrocatalysts under low-concentration  $\text{NO}_3^-$  conditions.

lower than that of  $\text{H-Co}_3\text{O}_4@\text{SRGA}$ , leading to the inference that SRGA with a nanoconfined effect can also contribute to the  $\text{eNO}_3^-$ -RR process. Notably,  $\text{Vo-HCo}_3\text{O}_4@\text{SRGA}$  also exhibited the smallest Tafel slope, indicating optimal reaction kinetics (Fig. S17a†). Subsequently, the  $\text{NH}_3$ -N yield rate of the catalysts was examined at different operating voltages, with  $\text{Vo-HCo}_3\text{O}_4@\text{SRGA}$  demonstrating the highest  $\text{NH}_3$ -N yield rate at all the corresponding voltages (Fig. 2b). The FE of  $\text{Vo-HCo}_3\text{O}_4@\text{SRGA}$  exhibited a volcano pattern with decreasing potential (Fig. 2c), indicating a certain starting potential is required for  $\text{NO}_3^-$  reduction to provide the driving force for the reaction. The subsequent FE decline at more negative potentials originates from the competing HER.<sup>29,30</sup> The FE of  $\text{Vo-HCo}_3\text{O}_4@\text{SRGA}$  was the highest at  $-0.8$  V vs. RHE (96.5%), corresponding to an  $\text{NH}_3$ -N yield rate of  $1.53$  mg  $\text{h}^{-1}$   $\text{cm}^{-2}$ . CV curves at different scan rates were analysed in a non-FE potential window (Fig. S17b-f†). The corresponding  $C_{dl}$  values are shown in Fig. 2d, in which the  $C_{dl}$  value of  $\text{Vo-HCo}_3\text{O}_4@\text{SRGA}$  is larger than that of  $\text{Y-Co}_3\text{O}_4@\text{SRGA}$ ,  $\text{H-Co}_3\text{O}_4@\text{SRGA}$  and  $\text{Co}@\text{SRGA}$ . Since the electrochemically active surface area is proportional to the value of  $C_{dl}$ , indicating that Vo increases the electrochemically active surface area, more active sites to facilitate the  $\text{eNO}_3^-$ -RR process are exposed. Furthermore, the  $C_{dl}$  value of  $\text{H-Co}_3\text{O}_4$  was only  $1.91$  mF  $\text{cm}^{-2}$  in comparison with  $\text{H-Co}_3\text{O}_4@\text{SRGA}$ , indicating that the nanoconfined effect of SRGA also facilitates enhancing the amount of active sites.  $\text{Vo-HCo}_3\text{O}_4@\text{SRGA}$  exhibited the smallest Nyquist circle diameter, implying that Vo promotes the electron transfer rate in the  $\text{eNO}_3^-$ -RR process (Fig. S18†). Further comparison of  $\text{H-Co}_3\text{O}_4$  and  $\text{H-Co}_3\text{O}_4@\text{SRGA}$  revealed that SRGA also accelerates the electron transfer rate to some extent. The product  $\text{NH}_3$ -N was verified to be derived from  $\text{NO}_3^-$ -N by designing blank control experiments with bare carbon paper, an open circuit potential, and no  $\text{NO}_3^-$  addition. The negligible  $\text{NH}_3$ -N yield rate under the conditions of the above blank control group experiments verified that the N in  $\text{NH}_3$  was derived from  $\text{NO}_3^-$ -N and not from other external contamination (Fig. S19†). The nitrogen changes and reaction processes were traced via  $^1\text{H}$ -nuclear magnetic resonance ( $^1\text{H}$ -NMR). The  $^1\text{H}$ -NMR peaks of  $^{15}\text{NH}_4^+$  and  $^{14}\text{NH}_4^+$  presented double and triple peaks when  $^{15}\text{NO}_3^-$  and  $^{14}\text{NO}_3^-$  were used as the N sources, further confirming that the  $\text{NH}_3$ -N does indeed originate from  $\text{NO}_3^-$ -N rather than from external sources of pollution (Fig. 2e).<sup>31</sup> Before advancing towards practical applications, the stability of the catalysts must be addressed. Fig. 2f illustrates the current *versus* time curves of  $\text{Vo-HCo}_3\text{O}_4@\text{SRGA}$  at different operating voltages, and the negligible current density decay indicates the appreciable stability of  $\text{Vo-HCo}_3\text{O}_4@\text{SRGA}$ . During 24 consecutive cycles, only the first three cycles revealed a reduced  $\text{NH}_3$ -N yield rate and FE decay, before remaining largely stable (Fig. 2g). The crystal structure and microscopic morphology showed no obvious change before and after the reaction (Fig. S20†), further illustrating the stability of the structure of  $\text{Vo-HCo}_3\text{O}_4@\text{SRGA}$  during the  $\text{eNO}_3^-$ -RR process. To investigate the suitability of  $\text{Vo-HCo}_3\text{O}_4@\text{SRGA}$  for different water qualities, the effects of different inorganic

anions, inorganic cations and HA on  $\text{NH}_3$ -N yield rate and FE were also investigated (Fig. S21†). Only a high concentration of  $\text{Mg}^{2+}$  (10 mM) inhibited the  $\text{NH}_3$ -N yield rate and FE, with no significant effect of other anions or even high concentrations of HA. In addition,  $\text{Vo-HCo}_3\text{O}_4@\text{SRGA}$  exhibited excellent activity in the pH range of 3–11 and  $\text{NO}_3^-$ -N of 50–500 mg  $\text{L}^{-1}$  (Fig. S22†). All these results indicated the potential applicability of  $\text{Vo-HCo}_3\text{O}_4@\text{SRGA}$  under real water conditions. Although the catalytic performance of  $\text{Vo-HCo}_3\text{O}_4@\text{SRGA}$  is greatly enhanced by defect and nanoconfined engineering, the difference in performance between  $\text{Vo-HCo}_3\text{O}_4@\text{SRGA}$  and other current state-of-the-art catalytic materials is unknown. Therefore, we summarized the performance of some advanced electrocatalytic systems reported in the literature at low concentrations of  $\text{NO}_3^-$  (Fig. 2h and Table S4†). Among these,  $\text{Vo-HCo}_3\text{O}_4@\text{SRGA}$  demonstrated the highest  $\text{NH}_3$ -N yield rate and FE, highlighting its superior performance as an  $\text{eNO}_3^-$ -RR electrocatalyst.

### 3.3. FEM and DFT investigation

The nanoconfined effect of SRGA on  $\text{NO}_3^-$  was successfully verified by finite element method (FEM) simulations (Fig. 3a and b and Fig. S23†). Compared with pure  $\text{Vo-HCo}_3\text{O}_4$ ,  $\text{SRGA}@\text{Vo-HCo}_3\text{O}_4$  was able to significantly enhance the localized concentration of  $\text{NO}_3^-$  due to the nanoconfined effect, thus greatly increasing the accessibility of  $\text{NO}_3^-$ . This nanoconfined effect contributes to the enhancement of  $\text{NO}_3^-$  activity in the  $\text{eNO}_3^-$ -RR *via* enriching the localized concentration of  $\text{NO}_3^-$ , which further facilitates its conversion process to  $\text{NH}_3$ . Electron localization function (ELF) calculations visualize that Vo formation induces a redistribution of the otherwise uniformly distributed electron density. This

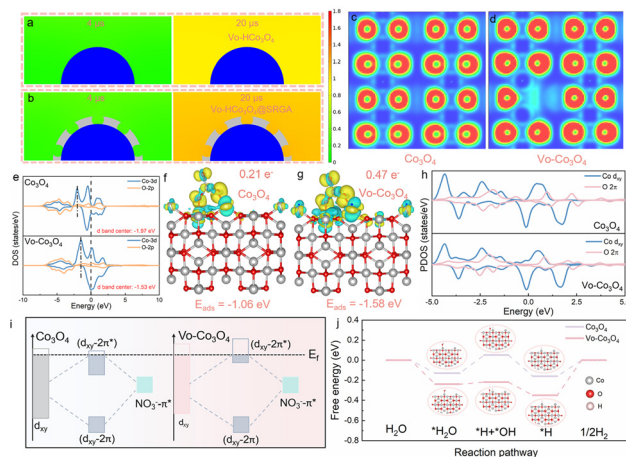


**Fig. 3** (a and b) Simulated concentration distribution of  $\text{NO}_3^-$  on the surface of  $\text{Vo-HCo}_3\text{O}_4$  and  $\text{Vo-HCo}_3\text{O}_4$  encapsulated with SRGA at different diffusion times. (c and d) ELF calculations, (e) DOS, (f and g) charge density difference, and (h) PDOS of  $\text{Co}_3\text{O}_4$  and  $\text{Vo-Co}_3\text{O}_4$ . (i) Spin-down PDOS orbital of  $d_{xy}-2\pi^*$  in  $\text{Co}_3\text{O}_4/\text{Vo-Co}_3\text{O}_4-\text{NO}_3^-$ . (j) Free-energy diagrams and corresponding reaction intermediates of water decomposition on  $\text{Co}_3\text{O}_4$  and  $\text{Vo-Co}_3\text{O}_4$ .

redistribution disrupts the original symmetry, generating a localized asymmetric electronic environment (Fig. 3c and d).<sup>32</sup>

Moreover, the Vo induced inhomogeneity in the Co–O bond length, further reflecting the disruption of the symmetry of the geometry (Fig. S24†). The location of the d-band center is an important theoretical basis for understanding the interaction between the catalyst surface and the reactants.<sup>33,34</sup> Vo raised the d-band center position of  $\text{Co}_3\text{O}_4$  to  $-1.53$  eV, leading to stronger electron exchange and  $\text{NO}_3^-$  adsorption (Fig. 3e). Further exploration is needed to elucidate the interaction between  $\text{NO}_3^-$  and the asymmetric defect sites. To investigate this, the adsorption configurations on the surfaces of  $\text{Co}_3\text{O}_4$  and  $\text{Vo-Co}_3\text{O}_4$  were constructed and analyzed (Fig. 3f and g). The adsorption energy ( $E_{\text{ads}}$ ) of  $\text{NO}_3^-$  on  $\text{Vo-Co}_3\text{O}_4$  ( $-1.58$  eV) was more negative than that of  $\text{Co}_3\text{O}_4$  ( $-1.06$  eV), and the charge transfer number between  $\text{NO}_3^-$  and  $\text{Vo-Co}_3\text{O}_4$  ( $0.47$  e $^-$ ) was higher compared to  $\text{Co}_3\text{O}_4$  ( $0.21$  e $^-$ ). These results demonstrated that Vo can strengthen  $\text{NO}_3^-$  adsorption and facilitate the electron transfer process.<sup>35</sup> The dense energy band structure of  $\text{Vo-Co}_3\text{O}_4$  implies a higher density of electronic states compared with  $\text{Co}_3\text{O}_4$ , contributing to a more efficient electron transfer with  $\text{NO}_3^-$  (Fig. S25†).<sup>36</sup> Accordingly, the interaction between adsorbed  $\text{NO}_3^-$  and the metal-centered orbitals of  $\text{Vo-Co}_3\text{O}_4$  was further explored. The  $d_{xy}$  orbital of Co and the  $2\pi$  orbitals of O in  $\text{NO}_3^-$  manifested a significant overlap in the partial density of states (PDOS) (Fig. 3h and Fig. S26†). This strong interaction triggers the splitting of the bonding and antibonding states. As the d-band center of  $\text{Vo-Co}_3\text{O}_4$  was close to the Fermi energy level, the  $d_{xy}$ – $2\pi^*$  energy levels of bonding and antibonding were subsequently elevated (\* represents the antibonding energy level) (Fig. 3i). In this case, the electron occupation of the antibonding state in the  $\text{NO}_3^-/\text{Vo-Co}_3\text{O}_4$  system decreased, enhancing the interaction between  $\text{NO}_3^-$  and  $\text{Vo-Co}_3\text{O}_4$ .<sup>37,38</sup> Fig. 3j and Fig. S27 and S28† show the Gibbs free energy change ( $\Delta G$ ) plots of  $\text{Co}_3\text{O}_4$  and  $\text{Vo-Co}_3\text{O}_4$  in the electrocatalytic HER and the optimized adsorption models of the corresponding intermediates. Vo drastically reduced the dissociation energy barrier of water molecules (0.22 eV to 0.05 eV), promoting easier dissociation of water molecules into  $\text{H}^+$  to provide the necessary intermediates for the reaction. In addition, the reaction energy barrier of  ${}^*\text{H} \rightarrow \text{H}_2$  for  $\text{Vo-Co}_3\text{O}_4$  (0.35 eV) was significantly higher than that for  $\text{Co}_3\text{O}_4$  (0.16 eV), indicating that Vo significantly inhibits the HER side reaction. In summary, the triple synergistic effect (enhanced  $\text{NO}_3^-$  adsorption, promoted  $\text{H}_2\text{O}$  dissociation, and effectively inhibited HER) of the Vo effectively ensures the high activity and selectivity of  $\text{Vo-Co}_3\text{O}_4$  in the  $\text{eNO}_3^-$ -RR process.

#### 3.4. Reaction mechanisms and pathway analysis

Two main mechanisms are commonly thought to drive the electrochemical reduction of  $\text{NO}_3^-$  to  $\text{NH}_3$ : direct electron transfer and bonding with  $\text{H}^+$ , and indirect reduction facilitated by  $\text{H}^*$ . The verification of whether  $\text{H}^*$  plays a dominant role in the  $\text{eNO}_3^-$ -RR was done by adding various concentrations of *tert*-butanol (TBA) as a scavenger. Even with the addition of excess TBA, there was no significant change in

$\text{NO}_3^-$  removal, thus ruling out the  $\text{H}^*$ -mediated pathway (Fig. 4a). Therefore, the main mechanism of  $\text{Vo-HCo}_3\text{O}_4@\text{SRGA}$  in the  $\text{eNO}_3^-$ -RR can be identified as direct electron transfer (Fig. 4b). The intermediate products adsorbed on the electrode surface were visualized using *in situ* FT-IR spectroscopy (Fig. 4c). There was no significant difference in the type of absorption peaks of  $\text{H-Co}_3\text{O}_4$ ,  $\text{H-Co}_3\text{O}_4@\text{SRGA}$ , and  $\text{Vo-HCo}_3\text{O}_4@\text{SRGA}$ , suggesting that the presence of SRGA and Vo does not alter the reaction intermediate products (Fig. 4d–f). The broad bands observed at  $1650\text{ cm}^{-1}$  and  $3300\text{ cm}^{-1}$  are the O–H bending vibrations of water adsorption ( $\delta\text{H–O–H}$ ) and cleavage ( $\nu\text{H–O–H}$ ),<sup>39,40</sup> while the bands located at around  $1458\text{ cm}^{-1}$  and  $1690\text{ cm}^{-1}$  belong to N–H and N–O stretching vibrations, confirming the formation of  $\text{NH}_3$  during the  $\text{eNO}_3^-$ -RR process.<sup>41,42</sup> Compared with  $\text{H-Co}_3\text{O}_4@\text{SRGA}$ ,  $\text{Vo-HCo}_3\text{O}_4@\text{SRGA}$  showed a more pronounced signal intensity change with  $\text{H}_2\text{O}$  and related intermediates at more negative potentials. This result suggests that Vo can facilitate  $\text{H}_2\text{O}$  dissociation and  $\text{NH}_3$  synthesis. Additionally, online DEMS further clarified that  $\text{Vo-HCo}_3\text{O}_4@\text{SRGA}$  generates intermediate products during the  $\text{eNO}_3^-$ -RR (Fig. 4g). The strongest  $m/z$  signal was 17, indicating that  $\text{Vo-HCo}_3\text{O}_4@\text{SRGA}$  is able to efficiently electrocatalyze the synthesis of  $\text{NH}_3$ . Several less intense  $m/z$  signals, such as 14, 15, 16, and 30, which correspond to  ${}^*\text{N}$ ,  ${}^*\text{NH}$ ,  ${}^*\text{NH}_2$ , and  ${}^*\text{NO}$  intermediates, confirm the occurrence of the  ${}^*\text{N}$  hydrogenation pathway. Combined with the above detected intermediates and previous reports, the reaction pathways can be deduced and used for theoretical calculations (Fig. S29†). Fig. 4h shows the  $\Delta G$  diagrams of  $\text{Co}_3\text{O}_4$  and  $\text{Vo-Co}_3\text{O}_4$  in the  $\text{eNO}_3^-$ -RR. For both  $\text{Co}_3\text{O}_4$  and  $\text{Vo-Co}_3\text{O}_4$ ,  $\text{NH}_3$  was synthesized by an 8-electron reduction of  $\text{NO}_3^-$  via

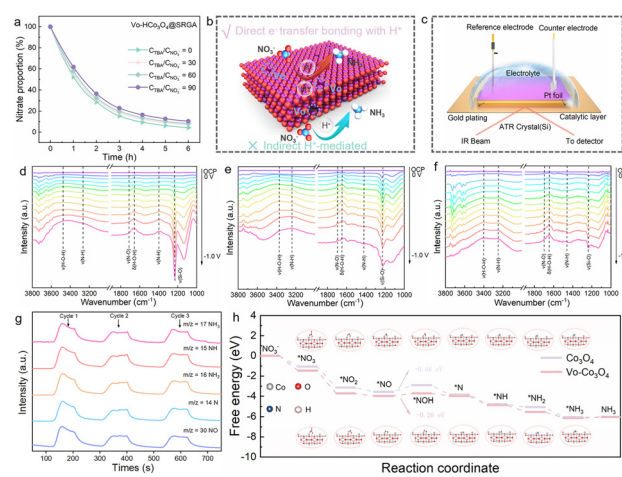


**Fig. 4** (a) Time profile of  $\text{NO}_3^-$  removal curves with or without the addition of TBA. (b) Mechanism schematic diagram of the  $\text{eNO}_3^-$ -RR on  $\text{Vo-HCo}_3\text{O}_4@\text{SRGA}$ . (c) Schematic illustration of the *in situ* electrochemical FT-IR. *In situ* FT-IR spectra of (d)  $\text{H-Co}_3\text{O}_4$ , (e)  $\text{H-Co}_3\text{O}_4@\text{SRGA}$ , and (f)  $\text{Vo-HCo}_3\text{O}_4@\text{SRGA}$  during the  $\text{eNO}_3^-$ -RR. (g) Online DEMS spectra of  $\text{Vo-HCo}_3\text{O}_4@\text{SRGA}$ . (h) Free-energy diagrams and corresponding reaction intermediates of the  $\text{eNO}_3^-$ -RR of  $\text{Co}_3\text{O}_4$  and  $\text{Vo-Co}_3\text{O}_4$ .

the pathway of  $\text{NO}_3^- \rightarrow *\text{NO}_3 \rightarrow *\text{NO}_2 \rightarrow *\text{NO} \rightarrow *\text{NOH} \rightarrow *\text{N} \rightarrow *\text{NH} \rightarrow *\text{NH}_2 \rightarrow *\text{NH}_3 \rightarrow \text{NH}_3$  (Fig. S30 and S31†).<sup>43,44</sup> During the whole reaction process, there are two steps with positive  $\Delta G$  values, which are the  $*\text{NO}$  hydrogenation ( $*\text{NO} \rightarrow *\text{NOH}$ ) and the desorption of  $*\text{NH}_3$  intermediates from the catalyst surface ( $*\text{NH}_3 \rightarrow \text{NH}_3$ ). Because of the high solubility of  $\text{NH}_3$  in aqueous solution and the low reaction energy barrier,  $\text{NH}_3$  can be readily desorbed from the surface of Co atoms, releasing additional reaction sites.<sup>45,46</sup> Therefore, the rate-determining step (RDS) of the  $\text{eNO}_3^-$ -RR can be considered as  $*\text{NO} \rightarrow *\text{NOH}$ . Obviously, Vo significantly reduced the reactive energy barrier of the RDS from 0.66 eV to 0.26 eV, improving the efficiency and selectivity of the  $\text{eNO}_3^-$ -RR.

## 4. Conclusions

In summary, we successfully anchored Vo-H<sub>2</sub>Co<sub>3</sub>O<sub>4</sub> obtained via the Kirkendall effect to the surface of SRGA. The porous skeleton of SRGA can improve the accessibility of the active sites. It also significantly increases the local  $\text{NO}_3^-$  concentration due to a unique nanoconfined effect, thereby accelerating the reaction kinetics. *In situ* FT-IR spectroscopy and DFT calculations demonstrate that Vo induced a triple synergistic modulation: enhancement of  $\text{NO}_3^-$  adsorption, promotion of water dissociation, and inhibition of the HER. Furthermore, the introduction of Vo raised the bonding and antibonding energy levels of  $d_{xy}-2\pi^*$  in  $\text{NO}_3^-/\text{Vo-Co}_3\text{O}_4$  and lowered the reaction energy barrier of RDS ( $*\text{NO} \rightarrow *\text{NOH}$ ), facilitating the adsorption and activation of  $\text{NO}_3^-$ . As a result, Vo-H<sub>2</sub>Co<sub>3</sub>O<sub>4</sub>@SRGA exhibited a considerable  $\text{NH}_3$ -N yield rate (1.53 mg h<sup>-1</sup> cm<sup>-2</sup>), Faraday efficiency (96.5%), and selectivity (97.2%) in the conversion of low-concentration  $\text{NO}_3^-$  to  $\text{NH}_3$ . This work highlights the design principles of advanced electrocatalysts for low-concentration  $\text{NO}_3^-$  conversion, providing solutions for resource recovery of  $\text{NO}_3^-$ -containing wastewater. We believe that this creative work has the opportunity to be extended to other electrocatalytic reactions in the aqueous phase, in addition to being generous in the  $\text{eNO}_3^-$ -RR.

## Author contributions

Ke Wang and Tong Zhao: data curation and writing – original draft. Shiyu Zhang: investigation. Rupeng Wang: formal analysis. Meng Wang: writing – review & editing. Zixiang He: supervision. Shih-Hsin Ho: funding acquisition.

## Data availability

The authors confirm that the data supporting the findings of this study are available within the article and its ESI.†

## Conflicts of interest

There are no conflicts to declare.

## Acknowledgements

This work was financially supported by the National Natural Science Foundation of China (No. 52070057).

## References

- 1 D. R. Kanter, O. Chodos, O. Nordland, M. Rutigliano and W. Winiwarter, *Nat. Sustainability*, 2020, **3**, 956–963.
- 2 B. Zhang, Z. Dai, Y. Chen, M. Cheng, H. Zhang, P. Feng, B. Ke, Y. Zhang and G. Zhang, *Nat. Commun.*, 2024, **15**, 2816.
- 3 J. Sun, S. Garg, J. Xie, C. Zhang and T. D. Waite, *Environ. Sci. Technol.*, 2022, **56**, 17298–17309.
- 4 F.-Y. Chen, Z.-Y. Wu, S. Gupta, D. J. Rivera, S. V. Lambeets, S. Pecaut, J. Y. T. Kim, P. Zhu, Y. Z. Finfrock, D. M. Meira, G. King, G. Gao, W. Xu, D. A. Cullen, H. Zhou, Y. Han, D. E. Perea, C. L. Muhich and H. Wang, *Nat. Nanotechnol.*, 2022, **17**, 759–767.
- 5 S. Han, H. Li, T. Li, F. Chen, R. Yang, Y. Yu and B. Zhang, *Nat. Catal.*, 2023, **6**, 402–414.
- 6 X. Chen, Y. Cheng, B. Zhang, J. Zhou and S. He, *Nat. Commun.*, 2024, **15**, 6278.
- 7 B. Zhou, Y. Tong, Y. Yao, W. Zhang, G. Zhan, Q. Zheng, W. Hou, X.-K. Gu and L. Zhang, *Proc. Natl. Acad. Sci. U. S. A.*, 2024, **121**, e2405236121.
- 8 W. Liao, J. Wang, G. Ni, K. Liu, C. Liu, S. Chen, Q. Wang, Y. Chen, T. Luo, X. Wang, Y. Wang, W. Li, T.-S. Chan, C. Ma, H. Li, Y. Liang, W. Liu, J. Fu, B. Xi and M. Liu, *Nat. Commun.*, 2024, **15**, 1264.
- 9 J. Suh, H. Choi, Y. Kong and J. Oh, *Adv. Sci.*, 2024, **11**, 2407250.
- 10 J.-J. Zhang, Y.-Y. Lou, Z. Wu, X. J. Huang and S.-G. Sun, *J. Am. Chem. Soc.*, 2024, **146**, 24966–24977.
- 11 N. C. Kani, N. H. L. Nguyen, K. Markel, R. R. Bhawnani, B. Shindel, K. Sharma, S. Kim, V. P. Dravid, V. Berry, J. A. Gauthier and M. R. Singh, *Adv. Energy Mater.*, 2023, **13**, 2204236.
- 12 K.-H. Kim, H. Lee, X. Huang, J. H. Choi, C. Chen, J. K. Kang and D. O'Hare, *Energy Environ. Sci.*, 2023, **16**, 663–672.
- 13 P. H. van Langevelde, I. Katsounaros and M. T. M. Koper, *Joule*, 2021, **5**, 290–294.
- 14 Y. Chen, M. Zuo, Y. Chen, P. Yu, X. Chen, X. Zhang, W. Yuan, Y. Wu, W. Zhu and Y. Zhao, *Nat. Commun.*, 2023, **14**, 5229.
- 15 Y. Huang, J. Ren and X. Qu, *Chem. Rev.*, 2019, **119**, 4357–4412.
- 16 J. Zhang, Z. Wang, X. Lin, X. Gao, Q. Wang, R. Huang, Y. Ruan, H. Xu, L. Tian, C. Ling, R. Shi, S. Xu, K. Chen and Y. Wu, *Angew. Chem., Int. Ed.*, 2025, **64**, e202416686.

17 W. Qu, M. Luo, Z. Tang, T. Zhong, H. Zhao, L. Hu, D. Xia, S. Tian, D. Shu and C. He, *Environ. Sci. Technol.*, 2023, **57**, 13205–13216.

18 S. Zhang, M. Sun, T. Hedtke, A. Deshmukh, X. Zhou, S. Weon, M. Elimelech and J.-H. Kim, *Environ. Sci. Technol.*, 2020, **54**, 10868–10875.

19 Q. V. Ly, L. Cui, M. B. Asif, W. Khan, L. D. Nghiem, Y. Hwang and Z. Zhang, *Water Res.*, 2023, **230**, 119577.

20 X. Zhang, J. Tang, L. Wang, C. Wang, L. Chen, X. Chen, J. Qian and B. Pan, *Nat. Commun.*, 2024, **15**, 917.

21 L. Wu, Z. Wang, J. Liu, C. Liu, X. Li, Y. Zhang, W. Wang, J. Ma and Z. Sun, *Appl. Catal., B*, 2024, **343**, 123526.

22 Q. Cheng, M. Huang, L. Xiao, S. Mou, X. Zhao, Y. Xie, G. Jiang, X. Jiang and F. Dong, *ACS Catal.*, 2023, **13**, 4021–4029.

23 W. Zhong, Z. Gong, Z. He, N. Zhang, X. Kang, X. Mao and Y. Chen, *J. Energy Chem.*, 2023, **78**, 211–221.

24 X. Chen, J. Chen, H. Chen, Q. Zhang, J. Li, J. Cui, Y. Sun, D. Wang, J. Ye and L. Liu, *Nat. Commun.*, 2023, **14**, 751.

25 Z. Wei, M. Zhao, Z. Yang, X. Duan, G. Jiang, G. Li, F. Zhang and Z. Hao, *Proc. Natl. Acad. Sci. U. S. A.*, 2023, **120**, e2217148120.

26 J. Zhu, W. Tu, H. Pan, H. Zhang, B. Liu, Y. Cheng, Z. Deng and H. Zhang, *ACS Nano*, 2020, **14**, 5780–5787.

27 D. Ji, L. Fan, L. Tao, Y. Sun, M. Li, G. Yang, T. Q. Tran, S. Ramakrishna and S. Guo, *Angew. Chem., Int. Ed.*, 2019, **58**, 13840–13844.

28 Y. Zhang, Y. Lin, T. Duan and L. Song, *Mater. Today*, 2021, **48**, 115–134.

29 K. Chu, W. Zong, G. Xue, H. Guo, J. Qin, H. Zhu, N. Zhang, Z. Tian, H. Dong, Y.-E. Miao, M. B. J. Roeffaers, J. Hofkens, F. Lai and T. Liu, *J. Am. Chem. Soc.*, 2023, **145**, 21387–21396.

30 Y. Xiong, Y. Wang, C. C. Tsang, J. Zhou, F. Hao, F. Liu, J. Wang, S. Xi, J. Zhao and Z. Fan, *Environ. Sci. Technol.*, 2024, **58**, 10863–10873.

31 Y. Wang, H. Li, W. Zhou, X. Zhang, B. Zhang and Y. Yu, *Angew. Chem., Int. Ed.*, 2022, **61**, e202202604.

32 W. Lyu, Y. Liu, J. Zhou, D. Chen, X. Zhao, R. Fang, F. Wang and Y. Li, *Angew. Chem., Int. Ed.*, 2023, **62**, e202310733.

33 S. Zhang, R. Wang, K. Wang, M. Wang, Z. He, H. Chen and S.-H. Ho, *Environ. Sci. Technol.*, 2024, **58**, 1921–1933.

34 L. Li, X. Zhang, M. Humayun, X. Xu, Z. Shang, Z. Li, M. F. Yuen, C. Hong, Z. Chen, J. Zeng, M. Bououdina, K. Temst, X. Wang and C. Wang, *ACS Nano*, 2024, **18**, 1214–1225.

35 K. Wang, R. Mao, R. Liu, J. Zhang, H. Zhao, W. Ran and X. Zhao, *Nat. Water*, 2023, **1**, 1068–1078.

36 H. Du, H. Guo, K. Wang, X. Du, B. A. Beshiwork, S. Sun, Y. Luo, Q. Liu, T. Li and X. Sun, *Angew. Chem.*, 2023, **135**, e202215782.

37 S. Yang, X. Guo, X. Li, T. Wu, L. Zou, Z. He, Q. Xu, J. Zheng, L. Chen, Q. Wang and Z. J. Xu, *Angew. Chem., Int. Ed.*, 2024, **63**, e202317957.

38 G. Qian, W. Lyu, X. Zhao, J. Zhou, R. Fang, F. Wang and Y. Li, *Angew. Chem., Int. Ed.*, 2022, **61**, e202210576.

39 M. Xie, G. Zhu, H. Yang, B. Liu, M. Li, C. Qi, L. Wang, W. Jiang, P. Qiu and W. Luo, *Adv. Energy Mater.*, 2024, **14**, 2401717.

40 J. Li, H. Li, K. Fan, J. Y. Lee, W. Xie and M. Shao, *Chem. Catal.*, 2023, **3**, 100638.

41 Y. Huang, C. He, C. Cheng, S. Han, M. He, Y. Wang, N. Meng, B. Zhang, Q. Lu and Y. Yu, *Nat. Commun.*, 2023, **14**, 7368.

42 J. Ni, J. Yan, F. Li, H. Qi, Q. Xu, C. Su, L. Sun, H. Sun, J. Ding and B. Liu, *Adv. Energy Mater.*, 2024, **14**, 2400065.

43 A. Zhu, H. Liu, S. Bu, K. Liu, C. Luan, D. Lin, G. Gan, Y. Zhou, T. Zhang, K. Liu, G. Hong, H. Li and W. Zhang, *ACS Nano*, 2024, **18**, 22344–22355.

44 S. Lu, G. Lin, H. Yan, Y. Li, T. Qi, Y. Li, S. Liang and L. Jiang, *ACS Catal.*, 2024, **14**, 14887–14894.

45 H. Y. Zhou, Y. B. Qu, J. C. Li, Z. L. Wang, C. C. Yang and Q. Jiang, *Appl. Catal., B*, 2022, **305**, 121023.

46 Z. Meng, J.-X. Yao, C.-N. Sun, X. Kang, R. Gao, H.-R. Li, B. Bi, Y.-F. Zhu, J.-M. Yan and Q. Jiang, *Adv. Energy Mater.*, 2022, **12**, 2202105.